

# Supplemental Material: Engineering the Topological Surface States in (Sb<sub>2</sub>)<sub>m</sub>-Sb<sub>2</sub>Te<sub>3</sub> Superlattice Series

J. C. Johannsen,<sup>1,\*</sup> G. Autès,<sup>2,3,\*</sup> A. Crepaldi,<sup>4,\*</sup> S. Moser,<sup>1</sup> B. Casarin,<sup>4,5</sup>  
F. Cilento,<sup>4</sup> M. Zacchigna,<sup>4</sup> H. Berger,<sup>1</sup> A. Magrez,<sup>1</sup> Ph. Bugnon,<sup>1</sup> J.  
Avila,<sup>6</sup> M. C. Asensio,<sup>6</sup> F. Parmigiani,<sup>4,5,7</sup> O. V. Yazyev,<sup>2,3</sup> and M. Grioni<sup>1,†</sup>

<sup>1</sup>*Institute of Condensed Matter Physics,  
Ecole Polytechnique Fédérale de Lausanne (EPFL), CH-1015 Lausanne, Switzerland*

<sup>2</sup>*Institute of Theoretical Physics, Ecole Polytechnique Fédérale  
de Lausanne (EPFL), CH-1015 Lausanne, Switzerland*

<sup>3</sup>*National Center for Computational Design and Discovery of Novel Materials MARVEL,  
Ecole Polytechnique Fédérale de Lausanne (EPFL), CH-1015 Lausanne, Switzerland*

<sup>4</sup>*Elettra - Sincrotrone Trieste S.C.p.A, Strada Statale 14,  
km 163.5, 34149 Basovizza, Trieste, Italy*

<sup>5</sup>*Università degli Studi di Trieste - Via A. Valerio 2, Trieste 34127, Italy*

<sup>6</sup>*Synchrotron SOLEIL, Saint Aubin, BP 48 F-91192 Gif-sur-Yvette, France*

<sup>7</sup>*International Faculty - University of Köln, 50937 Köln, Germany*

## I. Surface terminations

To complement the discussion in the main text, we provide here more details on the experimental identification of the surface terminations. The basic building blocks constituting the layered crystal structure of  $\text{Sb}_2\text{Te}_3$  consists of quintuple layers (QLs) stacked along the (0001) direction of the hexagonal unit cell, as shown in Fig. 1(a) of the main text. Each QL is formed by five covalently bonded atomic sheets in the order Te-Sb-Te-Sb-Te. While the interactions between the atomic sheets within a QL are strong, the interactions between two adjacent QLs are predominantly of weak van der Waals nature. As a consequence, the natural cleaving plane is located between the QLs and crystal cleaving thus always exposes a Te-terminated surface. In  $\text{Sb}_6\text{Te}_3$ , on the other hand, where two  $\text{Sb}_2$  bilayers (BLs) are sandwiched between the QLs, three different surface terminations can be envisaged upon cleavage, namely: a Sb-rich one-BL termination resulting from the breaking of the bonds between the two  $\text{Sb}_2$  BLs that are expected to have a significant covalent contribution [1]; a Sb-rich two-BL termination by breaking the weaker bonds to a neighboring QL; and a Te-terminated QL similar to that in  $\text{Sb}_2\text{Te}_3$ . These three cleavage planes are illustrated in Fig. S1(a) (see inset), where we also present representative core-level spectra of  $\text{Sb}_2\text{Te}_3$  and  $\text{Sb}_6\text{Te}_3$  collected over a range of binding energies covering the Te 4*d* and Sb 4*d* core levels.

The relative photoemission intensities of the Te 4*d* and Sb 4*d* core levels allow determining the surface termination. In the spectrum of  $\text{Sb}_2\text{Te}_3$  (green curve), we observe pronounced intensities from the Te 4*d* and Sb 4*d* core levels that, when corrected for the respective photoionization cross sections at the used photon energy of 75 eV [2], display approximately the same integrated intensity. This represents the spectral signature of a QL-terminated surface. All cleaved surfaces of  $\text{Sb}_2\text{Te}_3$  showed an identical core-level spectrum. For  $\text{Sb}_6\text{Te}_3$ , on the other hand, we observed spectral signatures of both the QL termination (blue curve) and, intriguingly, also a Sb-rich BL termination (red curve), as identified from the significantly larger (cross section corrected) intensity of the Sb 4*d* with respect to the Te 4*d* core levels. We note, however, that our data do not allow for a distinction between a one-BL termination and two-BL terminated surface. In a theoretical picture, the interactions between the  $\text{Sb}_2$  BLs are expected to be stronger than the bonds to the QL entity [1, 3]. As a result, we do expect the two-BL termination to be the most frequently occurring termination of the two. The observed shift of the Sb 4*d* levels to higher binding energies and the broadening of the spectral line shape are not fully understood. Although other explanations are

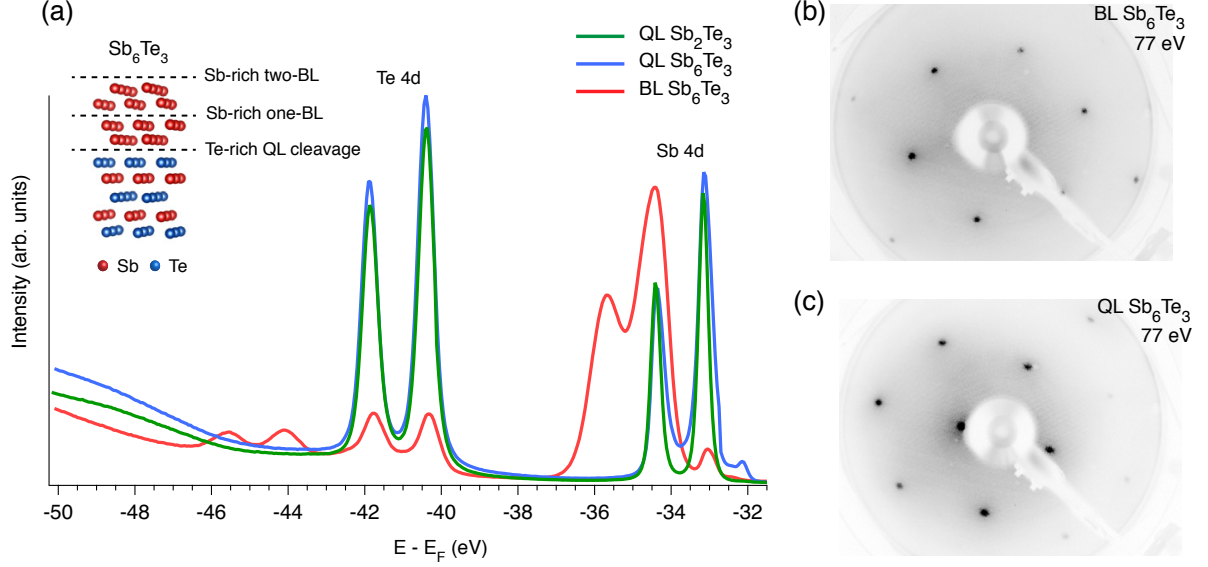


FIG. S1. (a) Normal emission photoemission intensity from Te 4d and Sb 4d core-levels measured with  $h\nu = 75$  eV at  $T = 100$  K on  $\text{Sb}_2\text{Te}_3$  (green), QL-terminated  $\text{Sb}_6\text{Te}_3$  (blue) and BL-terminated  $\text{Sb}_6\text{Te}_3$  (red). The left-hand inset shows a schematic illustration of different surface terminations in  $\text{Sb}_6\text{Te}_3$  with cleaving planes indicated by dashed horizontal lines. (b)-(c) Low-energy electron diffraction (LEED) patterns from BL and QL-terminated  $\text{Sb}_6\text{Te}_3$ , respectively, measured with an electron-beam energy of 77 eV. Both diffraction pattern display hexagonal symmetry.

also conceivable, as for instance surface segregation, we speculate that the shift and broadening might be the effect of a severe oxidation of the surface during crystal growth rather than a poorer crystalline quality of the surface. In fact, the low-energy electron diffraction (LEED) patterns in Fig. S1(b) and (c) display well-defined Bragg spots, which strongly suggests the existence of a two-dimensional long-ranged periodicity on both BL and QL terminations. A severe oxidation might also explain the double-peaked feature observed around  $E - E_F \approx -45$  eV. The separation in energy of the two peaks amounts to 1.45 eV that exactly corresponds to the splitting of the Te 4d spin orbit doublets observed around  $-41$  eV, thus indicating that the former peaks represent core-level shifts of oxidized Te 4d. We speculate that the contamination of the surface is so severe to the extent that the electronic states show no dispersion, as observed in all ARPES spectra acquired from Sb-rich terminated surfaces. As a final note, we reiterate that an oxidation is not the only conceivable explanation for the observed shift and broadening.

## II. Parabolic band dispersion of topological states in $\text{Sb}_6\text{Te}_3$

This section is devoted to providing more information about the dispersion of the topological surface states (TSS) in  $\text{Sb}_6\text{Te}_3$ . In Fig. S2(a), we reproduce the two-photon photoemission spectrum from Fig. 2(b) of the main text representing the dispersion of the TSS along the high-symmetry  $\bar{\Gamma} - \bar{K}$  direction. As noted in the main text, the dispersion of the TSS band displays a significant upper/lower branch asymmetry. In fact, this asymmetry in the dispersion relation for states belonging to the lower/upper branch is directly apparent already from a visual inspection of the data as presented in Fig. S2(a); in particular for  $k_{\parallel}$  from  $-0.05 \text{ \AA}^{-1}$  to  $-0.1 \text{ \AA}^{-1}$  (see red arrow). This observation is corroborated by a more quantitative analysis of the ARPES spectrum utilizing momentum (MDC) and energy (EDC) distribution curves that correspond to constant energy and momentum cuts, respectively, to the data. The results of this analysis is shown in Fig. S2(b) where we have superimposed the fitted peak positions of the extracted EDCs and MDCs for the lower and upper band, respectively. We observe that the dispersion relation (blue) of the lower band of TSS indeed deviates strongly from the linear relationship (red) characterizing the upper band along the same high-symmetry direction. As explained in the main tex, this is in excellent qualitative agreement with our first-principle band structure calculations.

The choice of EDCs (MDCs) for the lower (upper) TSS band to track the dispersion along the high-symmetry direction is explained by the flat parabolic (linear) dispersive character of the band. In the extreme limit where the band displays no dispersion with momentum, an EDC analysis is the only way to extract the position of the quasiparticle peak at a given point in momentum space. The MDC (EDC) peak position were determined from fits to a Lorentzian (Gaussian) function and a polynomial background. The MDC and EDC representation of the spectrum used for the analysis are shown in Fig. S2(c) and (d), respectively. For the reader's convenience, a red arrow has been added to point out the position of the lower TSS band in the spectra.

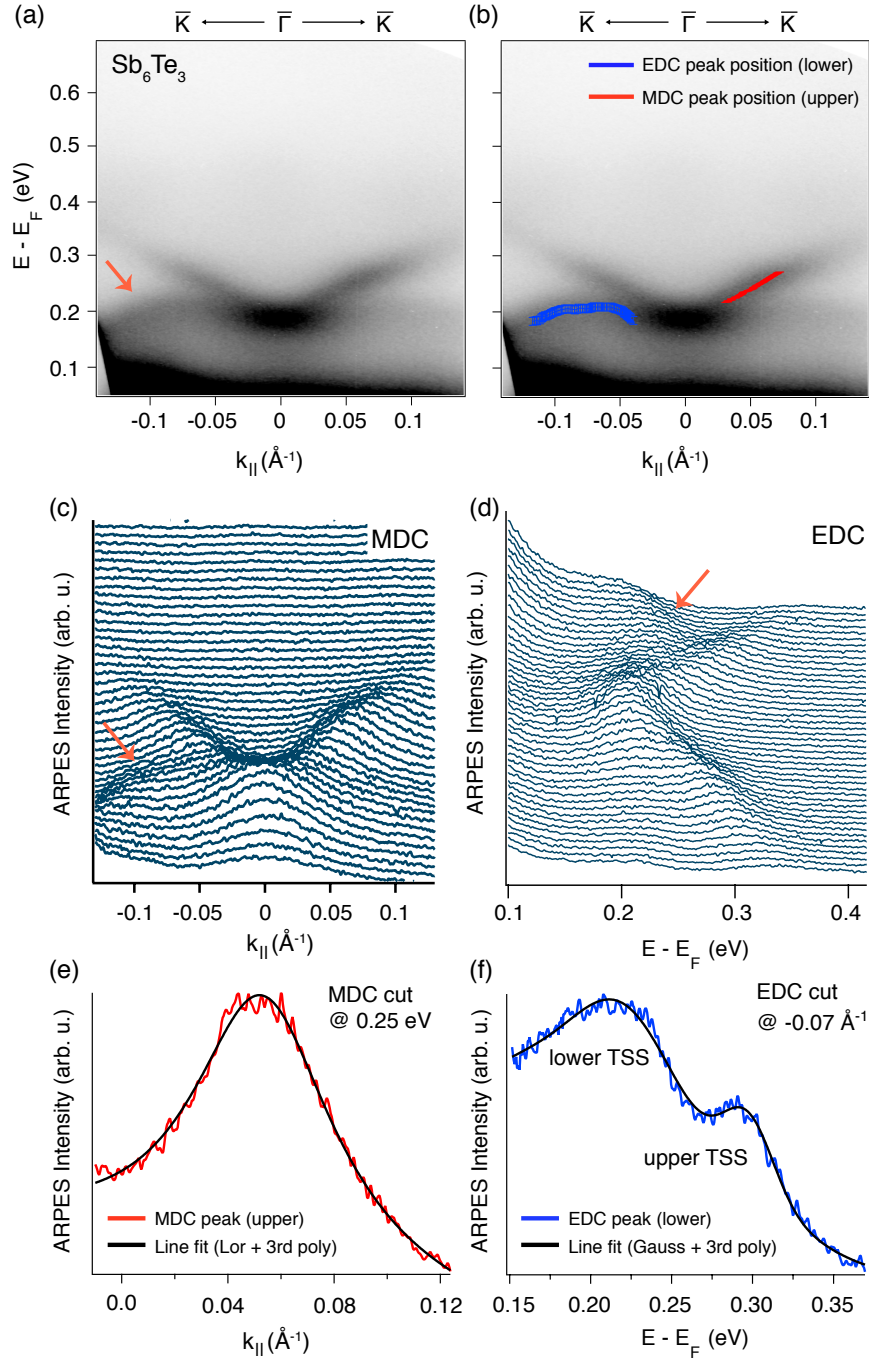


FIG. S2. Extraction of the TSS band dispersion in  $\text{Sb}_6\text{Te}_3$ . (a) Two-photon photoemission intensity map along  $\bar{\Gamma} - \bar{K}$  of the Te-terminated surface Brillouin zone measured with pump energy of 1.55 eV and probe energy of 6.20 eV at room temperature. (b) Same spectrum as in (a) but with the determined MDC and EDC peak positions of the upper and lower TSS branch imposed on the experimental map. (c) and (d) The spectrum decomposed into MDCs and EDCs, respectively. Red arrows have been added to point out the region in momentum space where the lower TSS band disperses. (e) and (f) A single MDC and EDC cut, respectively, taken at the indicated binding energy and crystal momentum. In the case of the MDC (EDC), the fit was performed by a Lorentzian (Gaussian) line profile and third-order polynomial.

### III. Calculated electronic structure of Sb<sub>2</sub>-terminated Sb<sub>6</sub>Te<sub>3</sub>

Motivated by the existence of Sb-rich BL terminated surfaces upon cleaving Sb<sub>6</sub>Te<sub>3</sub>, we have calculated the electronic band structures of the three possible terminations, i.e. the Te-rich QL termination [Fig. S3(a)], the Sb-rich one-BL termination [Fig. S3(b)] and the Sb-rich two-BL termination [Fig. S3(c)]. Firstly, we note that the Dirac point (DP) energy displays a strong dependence on the surface termination with the DP located at higher energies when the slab is terminated by one-BL or two-BL. These results are in good agreement with the calculations of the pure Sb and Sb<sub>2</sub>Te<sub>3</sub> slabs [Fig. 3 of the main text] that show that the DP is located closer to the conduction band in the case of pure Sb. Secondly, the results show that also the nature of the additional surface state located around  $E - E_F = -0.8$  eV in another gap of the projected bulk valence band continuum at  $\bar{\Gamma}$ . While the QL termination here exhibits a spin-orbit split Rashba state (as mentioned in the main text and discussed in more detail below), no Rashba-split surface state is observed for the one-BL termination. The two-BL termination, on the other hand, does host a surface state with a Rashba-split upper branch.

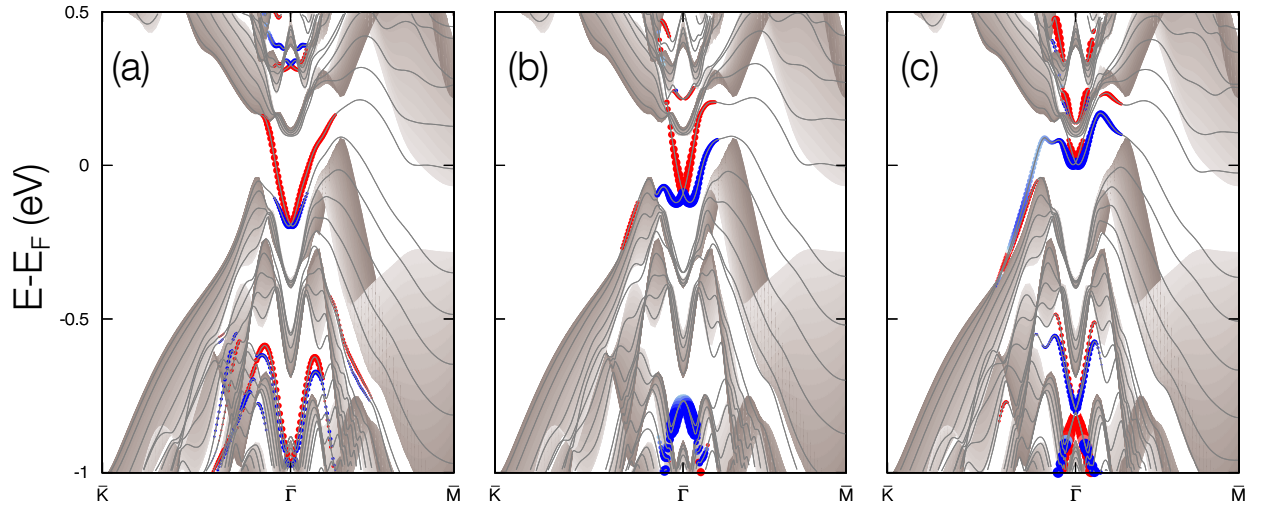


FIG. S3. Calculated electronic band structures for slab models (lines) of Sb<sub>6</sub>Te<sub>3</sub> with (a) Te-rich QL, (b) Sb-rich one-BL and (c) Sb-rich two-BL terminations, superimposed to the projected bulk states (grey shading). The surface-localized states are depicted in red and blue indicating clockwise and counter-clockwise helicity of the in-plane spin polarization, respectively.

#### IV. Hexagonal warping and the out-of-plane spin polarization

We investigated theoretically the degree of hexagonal warping of TSS in  $\text{Sb}_2\text{Te}_3$  and  $\text{Sb}_6\text{Te}_3$ , which was evaluated as  $k_{\bar{\Gamma}-\bar{K}}/k_{\bar{\Gamma}-\bar{M}}$  for the upper TSS branch at a given energy [Fig. S4(a)]. Close to the Dirac energy and the  $\bar{\Gamma}$  point, the TSS band dispersion is isotropic with  $k_{\bar{\Gamma}-\bar{K}}/k_{\bar{\Gamma}-\bar{M}} \approx 1$ . Away from the  $\bar{\Gamma}$  point, the constant energy contours are warped [Fig. S4(b)] and the ratio  $k_{\bar{\Gamma}-\bar{K}}/k_{\bar{\Gamma}-\bar{M}}$  decreases. The hexagonal warping of the TSS is related to the emergence of an out-of-plane component of the spin polarization [7]. Figure S4(a) shows the absolute value of the out-of-plane spin component for  $k_{\parallel}$  along the  $\bar{\Gamma} - \bar{K}$  direction. Close to the Dirac point, where the TSS is isotropic, the out-of-plane spin component is zero. At higher energy, where the contours are significantly warped, the out-of-plane spin polarization along the  $\bar{\Gamma} - \bar{K}$  direction increases reaching 0.35 and 0.43 at  $E = 0.25$  eV above the Dirac point for  $\text{Sb}_2\text{Te}_3$  and  $\text{Sb}_6\text{Te}_3$ , respectively. The complete spin texture of the out-of-plane spin component in reciprocal space is shown schematically in Fig. S4(b). At a given energy, the absolute value of the out-of-plane spin polarization is maximal along the three  $\bar{\Gamma} - \bar{K}$  directions and oscillates between positive and negative orientation around the constant energy contour, while it cancels along the three  $\bar{\Gamma} - \bar{M}$  directions that coincide with the mirror symmetry planes [7]. In contrast, the in-plane spin polarization is fairly constant along the whole energy range of the upper part of the TSS with a value of  $\approx 0.6$  and a clockwise helicity. These results demonstrate a strong tunability of the spin properties of the TSS.

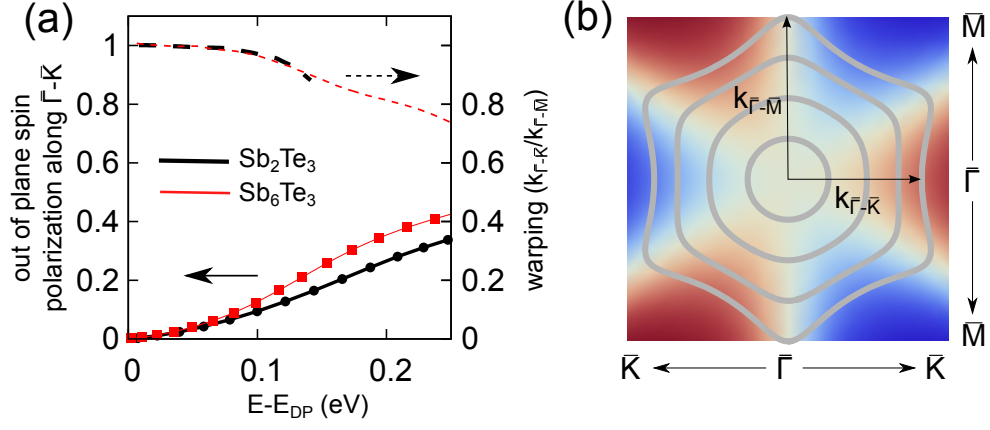


FIG. S4. (a) Out-of-plane polarization of the upper branch of the TSS band along the  $\bar{\Gamma} - \bar{K}$  direction (solid line) and intensity of the hexagonal warping  $k_{\bar{\Gamma}-\bar{K}}/k_{\bar{\Gamma}-\bar{M}}$  for  $\text{Sb}_2\text{Te}_3$  and  $\text{Sb}_6\text{Te}_3$  as a function of energy relative to the Dirac point. (b) Schematic representation of the TSS constant energy contours (grey lines) and out-of-plane spin polarization (red for positive and blue for negative).



## V. Topological invariants

The crystal structures of the  $(\text{Sb}_2)_m\text{-Sb}_2\text{Te}_3$  family compounds belong to either the rhombohedral space group  $R\bar{3}m$  (166) (for  $m = 3p$  or  $3p + 1$ ) or the primitive hexagonal space group  $P\bar{3}m1$  (164) (for  $m = 3p + 2$ ) [5].  $\text{Sb}_2\text{Te}_3$ ,  $\text{Sb}_4\text{Te}_3$ ,  $\text{Sb}_8\text{Te}_3$  are rhombohedral, while  $\text{Sb}_6\text{Te}_3$  is hexagonal.

Since these crystals are centrosymmetric, the  $Z_2$  topological invariants can easily be computed from the DFT band structures following the method described by Fu and Mele [4]. We first compute for each time-reversal invariant momentum (TRIM) point  $\Lambda$  in the 3D BZ the quantities

$$\delta_\Lambda = \prod_{i=1}^{N/2} \xi_{2i}(\Lambda), \quad (1)$$

where  $\xi_{2i} = \xi_{2i+1}$  is the parity eigenvalue of the occupied degenerate bands  $2i$  and  $2i + 1$ . The values of  $\delta_\Lambda$  for the  $\beta$ -phase are reported in Table I. A change of sign of  $\delta$  between two TRIM points reveals the presence of a band inversion. The strong topological invariant  $\nu_0$  is given by  $(-1)^{\nu_0} = \prod_{\Lambda} \delta_\Lambda$  and is non-zero if there is an odd number of band inversions in the 3D BZ. The weak invariants are obtained from the product of 4  $\delta_\Lambda$  at 4 coplanar TRIM points in the Brillouin zone ( $\nu_1 = \nu_2 = \nu_3 = \delta_Z \delta_L \delta_F \delta_F$  for the rhombohedral structure and  $\nu_1 = \nu_2 = \delta_M \delta_M \delta_L \delta_L$ ,  $\nu_3 = \delta_A \delta_L \delta_L \delta_L$  for the primitive hexagonal structure).

The values of  $\delta_\Lambda$  and the corresponding topological invariants are reported in Table I for the four members of the series  $\text{Sb}_2\text{Te}_3$ ,  $\text{Sb}_4\text{Te}_3$ ,  $\text{Sb}_6\text{Te}_3$  and  $\text{Sb}_8\text{Te}_3$ . The four compounds have a non-zero strong invariant which indicates that topologically protected surface states are present on each of their surface. The weak invariants, which provide information about the positions of the Dirac cones in the surface Brillouin zone, alternate across the series between (1,000) for  $\text{Sb}_2\text{Te}_3$  and  $\text{Sb}_6\text{Te}_3$  and (1,111) for  $\text{Sb}_4\text{Te}_3$  and  $\text{Sb}_8\text{Te}_3$ . Nevertheless, since the  $\Gamma = (0, 0, 0)$  point and the rhombohedral  $Z = (\frac{1}{2}, \frac{1}{2}, \frac{1}{2})$  point both project onto the  $\bar{\Gamma}$  point in the (0001) surface 2D Brillouin zone, this distinction is not apparent for the experimentally relevant (0001) surface. Both topological phases lead to a TSS Dirac cone at  $\bar{\Gamma}$ . The alternation of the weak indices would be apparent if side surfaces were experimentally accessible.

TABLE I. Values of  $\delta_\Lambda$  at the 8 TRIM points and  $Z_2$  topological invariants. See Fig. S5 for the definition of positions of the TRIM points in the rhombohedral and hexagonal bulk Brillouin zones.

$R\bar{3}m (P\bar{3}m1)$	$\text{Sb}_2\text{Te}_3(\text{R})$	$\text{Sb}_4\text{Te}_3(\text{R})$	$\text{Sb}_6\text{Te}_3(\text{P})$	$\text{Sb}_8\text{Te}_3(\text{R})$
$\Gamma$	-1	1	-1	1
$Z (A)$	1	-1	1	-1
$3L (3M)$	1	1	1	1
$3F (3L)$	1	1	1	1
$(\nu_0, \nu_1 \nu_2 \nu_3)$	(1,000)	(1,111)	(1,000)	(1,111)

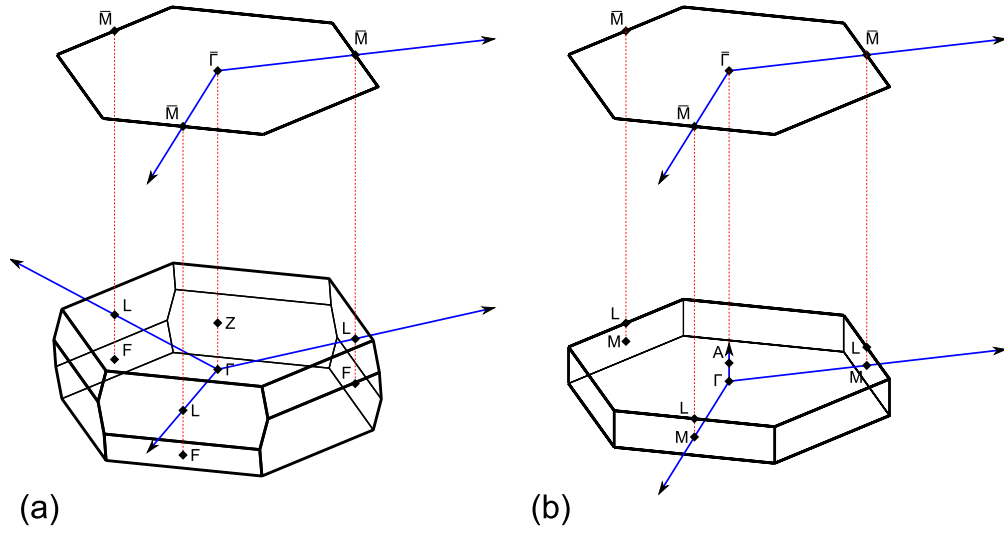


FIG. S5. Brillouin zones corresponding to (a) the rhombohedral and (b) the hexagonal crystal structures showing the position of the 8 TRIM points and their projection on the (0001) surface 2D Brillouin zone.

## VI. Probing the $k_z$ -dependence of the low-energy states in $\text{Sb}_2\text{Te}_3$

In this section, we present a discussion of the  $k_z$ -dependence of the low-energy states of  $\text{Sb}_2\text{Te}_3$  and arguments supporting the two-dimensional (2D) nature of some of these states.

In an ARPES experiment, the 2D character of electronic states manifests itself in an absence of dispersion along  $k_z$ . The  $k_z$ -dependence of the states can be assessed by varying the photon energy. The acquired photoemission intensity of the states as a function of photon energy is thereafter transformed using the following relationship relating the  $k_z$  values to the kinetic energy  $E_{\text{kin}}$  of the detected photoelectrons, the constant inner potential  $V_0$  and the emission angle  $\Theta$ :

$$k_z = \sqrt{\frac{2m_e}{\hbar^2}(V_0 + E_{\text{kin}}\cos(\Theta)^2)} \quad (2)$$

The transformation relies on the assumption that the final states in the photoemission process are simple free electron states, an approximation that in most cases delivers the required precision. Fig. S6(a) shows an ARPES spectrum of the low-energy band structure of  $\text{Sb}_2\text{Te}_3$  along the  $\bar{\Gamma} - \bar{K}$  direction acquired using a photon energy of 66 eV. In Fig. S6(b) and (c), we probe the  $k_z$ -dependence of the states with the  $k_{\parallel}$  values indicated by the blue ( $0.35 \text{ \AA}^{-1}$ ) and green ( $-0.075 \text{ \AA}^{-1}$ ) dashed vertical lines, respectively, in Fig. S6(a). For the measured state A in Fig. S6(b) (blue line), we observed a clear  $k_z$ -dependence of the dispersion, pointing to a bulk nature of this state. This is in contrast to the measured state B in Fig. S6(c) (green line) that is located in close vicinity to the Fermi level and which does not display any significant dispersion in  $k_z$ ; a result that strongly suggest a 2D confined state. In fact, a comparison of the data with the first-principles calculation of the electronic band structure of  $\text{Sb}_2\text{Te}_3$  (see inset to Fig. S6(a)) suggests that the Fermi level of the  $\text{Sb}_2\text{Te}_3$  crystal is located in the lower branch of the Dirac cone of the topological surface states. Taken together, these results suggest that the states in close vicinity to the Fermi level for this compound are indeed surface states, as also reported by another recent ARPES study [6].

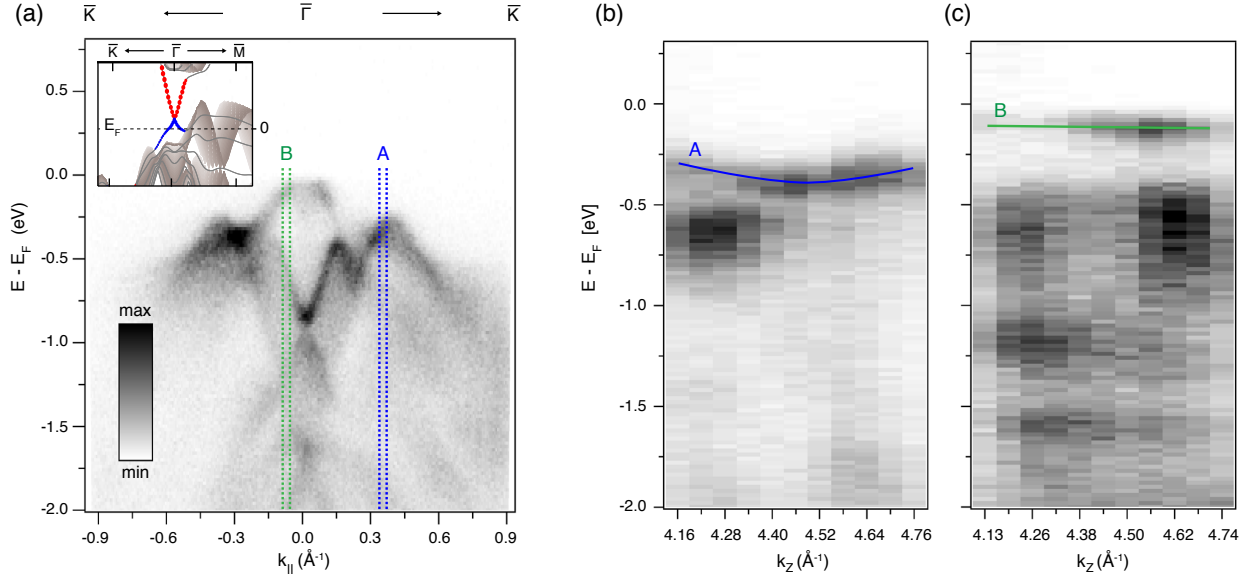


FIG. S6. (a) Photoemission intensity from the states along  $\bar{\Gamma} - \bar{K}$  of the first surface Brillouin zone of  $\text{Sb}_2\text{Te}_3$  measured with a photon energy of 66 eV. The inset display the calculated electronic structure. A comparison with the experimental data shows that the experimental Fermi level is located in the lower branch of the Dirac cone. The blue ( $k_{\parallel} = 0.35 \text{ \AA}^{-1}$ ) and green ( $k_{\parallel} = 0.075 \text{ \AA}^{-1}$ ) vertical lines indicates the  $k_{\parallel}$  values (binned over a small window of  $\pm 0.01 \text{ \AA}^{-1}$ ) of the states whose dispersion in  $k_z$  is assessed in (b) and (c), respectively. (b)-(c) Photon energy scan illustrating the dispersion of the states at the  $k_{\parallel}$  values indicated by the blue and green line, respectively, in (a). The horizontal axis has be transformed to  $k_z$  values instead of photon energies using Eq. (1). In the transformation, we assumed a constant inner potential of  $V_0 = 10 \text{ eV}$ . The photon energy scan spanned the energies from 60 to 80 eV in steps of 2 eV.

## VII. Discerning the Rashba-split surface state

In Fig. 1(c) of the main text, we show that the electronic structure of  $\text{Sb}_2\text{Te}_3$  exhibits a spin-split Rashba-type surface state in a gap of the projected bulk valence band at the  $\bar{\Gamma}$  point 0.6 eV below the Fermi level. The existence of this additional surface state originating from spin-orbit interactions has also been identified in a recent spin-resolved ARPES study [6]. The direct observation by ARPES has, however, not been reported hitherto in the literature. Here, we demonstrate that we are able to discern the two Rashba branches directly in the ARPES data, and provide an estimate of the effective mass  $m^*$  and Rashba parameter  $\alpha$  that characterize the dispersion of the two branches:

$$E_{\pm} = \frac{\hbar^2}{2m^*} \mathbf{k}_{\parallel}^2 \pm \alpha |\mathbf{k}_{\parallel}| \quad (3)$$

In Fig. S7(a), we show an ARPES spectrum measured along the  $\bar{M} - \bar{\Gamma} - \bar{K}$  direction of the first Brillouin zone of  $\text{Sb}_2\text{Te}_3$  using a photon energy of  $h\nu = 76$  eV. For energies  $E - E_F = -0.4 - -0.8$  eV, two sets of parabolic bands (split in energy and  $k$ ) are clearly discernible along  $\bar{\Gamma} - \bar{K}$ , whereas no such splitting can be identified along  $\bar{\Gamma} - \bar{M}$ . Each band is shown to have its maximal binding energy at about 800 meV.

A more quantitative analysis is provided in Fig. S7(b) and (c). In Fig. S7(c), we show a single momentum distribution curve (MDC) at a fixed energy of 0.68 eV below  $E_F$ , as indicated by the green arrows in Fig. S7(b). We ascribe the two well-separated peaks located around  $k_{\parallel} = 0.07 \text{ \AA}^{-1}$  to the two spin-split Rashba branches. The dispersion of these branches can be estimated by tracking the peak position of the MDC line shape for cuts performed at different energies. The result of such an analysis is presented in Fig. S7(b), where the MDC peak dispersions have been superimposed with the ARPES spectrum. Fitting the determined dispersion by the Rashba model in Eq. (2) gives coarse estimates of the effective mass  $m^* = 0.05(4)m_e$  and the Rashba parameter  $\alpha = 1.5(3) \text{ eV\AA}$ .

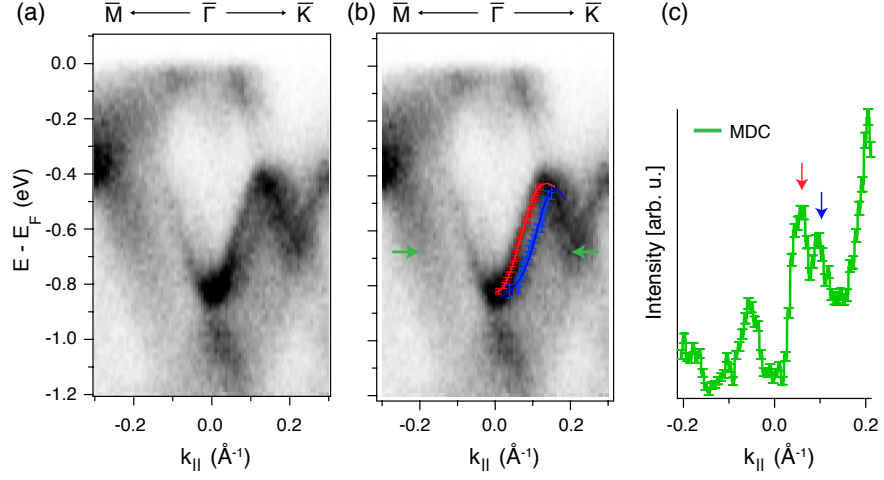


FIG. S7. (a) Photoemission intensity along the  $\bar{M} - \bar{\Gamma} - \bar{K}$  direction of the first surface Brillouin zone of  $\text{Sb}_2\text{Te}_3$  measured with a photon energy of 76 eV. (b) Same raw ARPES spectrum as in (a). The extracted MDC peak dispersions of the Rashba branches have been superimposed to the image together with the results (solid lines) of the fits of the Rashba model in Eq. (2). (c) Momentum distribution curve (covering momenta from  $-0.2 \text{ \AA}^{-1}$  to  $+0.2 \text{ \AA}^{-1}$ ) at a fixed energy of  $E - E_F = -0.68$  eV, as indicated by the green arrows in (b).

---

\* These authors contributed equally to the work.

† E-mail address: marco.grioni@epfl.ch

- [1] H. Lind, S. Lidin, and U. Häussermann, *Phys. Rev. B* **72**, 184101 (2005).
- [2] J. J. Yeh and I. Lindau, *At. Data. Nucl. Data Tables* **32**, 155 (1985).
- [3] J. W. G. Bos, H. W. Zandbergen, M.-H. Lee, N. P. Ong, and R. J. Cava, *Phys. Rev. B* **75**, 195203 (2007).
- [4] L. Fu and C. L. Mele, *Phys. Rev. B* **76**, 045302 (2007).
- [5] K. Kifune, Y. Kubota, T. Matsunaga, and N. Yamada, *Acta Cryst. B* **61**, 492 (2005).
- [6] C. Pauly, G. Bihlmayer, M. Liebmann, M. Grob, A. Georgi, D. Subramaniam, M. R. Scholz, J. Sánchez-Barriga, A. Varykhalov, S. Blügel, O. Rader, and M. Morgenstern, *Phys. Rev. B* **86**, 235106 (2012).
- [7] L. Fu, *Phys. Rev. Lett.* **103**, 266801 (2009).